THREE-DIMENSIONAL SIMULATIONS OF INSTABILITIES IN ACCRETION DISK TORUS

Jung Lin (Doris) Lee

ABSTRACT

Accretion disks can be found in a variety of astrophysical systems, such as around young stars and black holes. It has been long proposed that fluid instabilities can generate the turbulent viscosity required for driving outward angular momentum transport in accretion flows. In this project, we investigate the dynamics of an accretion disk torus using the new magnetohydrodynamics (MHD) code, *Athena++* . First, we examine the hydrodynamical behavior of the torus when perturbed by small non-axisymmetric modes and show that it gives rise to a global fluid instability known as the Papaloizou-Pringle Instability (PPI). We numerically simulate a slender torus and track its evolution into non-linear regimes. We experiment with various physical and numerical parameters to explore how it affects the torus simulation. By computing the mode amplitude in the linear regime before saturation, we can quantify the mode growth and compare the results with the predicted analytical mode growth. Then, we investigate the behavior of a torus initialized with a weak toroidal magnetic field and examine the effects of magnetorotational instability (MRI). Using high-resolution simulations, we are able to resolve the higher order modes of the MRI. We computed the mass accretion history of the instabilities and found that MRI is significantly more effective in transporting the angular momentum outward than compared to PPI. Convergence with previous results in literature demonstrates the robustness of *Athena++* in handling both types of instabilities in accretion disk tori.

Keywords: instabilities, hydrodynamics, methods:numerical, accretion:accretion disks

1. INTRODUCTION

Accretion disks can be found in a wide variety of astrophysical systems and size scales from protostellar disks around young stars to galactic discs around AGNs. If angular momentum is conserved in these systems, it is necessary for the angular momentum to transport outward in order for material from the disc to accrete onto the central object. One of the central questions in accretion disc physics is the possible mechanisms that enable outward angular momentum transport in discs. Observational signatures of high-energy jets and outflows are evidence of such transport at work. On the theoretical front, most of the efforts have been directed towards the development of better numerical scheme and codes to realistically simulate such systems.

In this project, we use the new hydrodynamic, magnetohydrodynamics (MHD) code, *Athena++* , to study two types of fluid instabilities in accretion disk tori. The first is the Papaloizou-Pringle Instability (PPI), a type of global, hydrodynamical instability that occurs in accretion tori with constant angular momentum throughout. The second instability we examined is the MRI, which is a local, MHD instability that has gained considerable recent interest due to its effectiveness in providing outward angular momentum transport in the disc.

In Section 1, I will describe how we initialize the PPI simulation and the numerical methods that we use to simulate these systems. Section 2 details the basics setup for our MRI study and explore the effects of changing the grid resolutions. Finally, Section 3 highlights the nature of these instabilities by comparing their mode growth and mass accretion rate history.

2. PAPALOIZOU PRINGLE INSTABILITY

An accretion tori can be realized in accretion disk near its Eddginton luminosity, where the torus is in hydrostatic equilibrium between radiation pressure and inward gravitational force. In high accretion rate or high energy systems, such as AGNs and qusars, radiation near the poles creates a hollow region near the central accreting object and results in the toroidal geometry. In scenarios of discs with very high internal temperature, the pressure gradient can get so large that the rotational profile deviate significantly from a Keplerian disk. In Papaloizou and Pringle (1984), the authors consider a torus with a rotational velocity profile that sets up a constant angular momentum. By conducting a linear stability analysis, they found that non-axisymmetric perturbations result in exponential mode growth on the order of dynamical timescale, resulting in the global, hydrodynamical instability known as the Papaloizou-Pringle Instability (PPI). Further studies conducts linear stability analysis of the case of the slender torus using a set of 2D height-averaged equations. These are applicable when examining lower order modes on the principal branch where the scaled azimuthal wavenumber $\beta < 0.59$, since the torus is in vertical hydrostatic equilibrium. [1]

However, linear stability analysis breaks down after Papaloizou-Pringle instability arises and the system becomes nonlinear. In this nonlinear regime, three-dimensional numerical simulations are required to track the evolution of the torus. Hawley (1990) found that the instability breaks the torus up into independent "planets" , which is a more stable configuration than the instabilities in the torus. Even though the PPI was originally proposed as a possible mechanism for generating the turbulent viscosity required for outward angular momentum transport, it is not as effective as the MRI and requires an idealized initial setup for the instability to occur that is unlikely to realize astrohphysical settings.

Nevertheless, the PPI is still of academic interest in our study since there exist an analytical prediction for the mode growth Goldreich et al. (1986), therefore it serves as a well-studied test case to with which we could compare the results of our *Athena++* simulations. As noted in Hawley (1991), numerical diffusion tends to suppress mode growth and stabilizes the torus. Therefore,

[1] The more general case of a non-uniform angular momentum torus is studied in Papaloizou and Pringle (1985) which additionally give rise to Kelvin-Helmholtz-like instabilities.

this serves as a robust test case for the hydrodynamics scheme in *Athena++* . In this project, we reproduce the Hawley's 3D finite difference simulation with a higher grid resolution and using more accurate hydrodynamics schemes in the new *Athena++* code.

2.1. *Numerical Methods*

To observe the effects of how the instability is affected by different parameters, we first conducted a series of low resolution (64^3) numerical experiments to qualitatively examine the behavior of the m=1 mode. In order to track its evolution, the simulations are carried out far into the nonlinear regime until the pressure maximum spirals into the innermost boundary. The results are summarized in Table 1. R_0/R_B, the ratio between the radius to pressure maximum and to inner boundary, defines the radial dynamic range of the grid. All the models uses an adiabatic equation of state where γ=5/3. t_{run} is denoted in units of orbits. The computation is carried out on Hopper, NERSC's Cray XE6 System and Edison, a Cray XC30 System.

2.1.1. *Initial Conditions*

As derived in Papaloizou and Pringle (1984), the initial conditions of the torus satisfies hydrostatic equilibrium.

$$-\frac{\nabla P}{\rho} - \nabla\psi_{pm} + \Omega^2\tilde{\omega}\hat{\tilde{\omega}} = 0 \quad (1)$$

where ψ_{pm} is the pseudo-Newtonian potential used in Blaes (1987)

$$\phi = \frac{-GM}{r - R_G} \quad (2)$$

Here we approximate the Schwarzschild radius $R_G = 0$ since $R_G << R_0$ of the torus. The torus density that satisfies this condition is given by:

$$\rho(r,\theta) = \left[\frac{GM}{(n+1)AR_0}\left[\frac{R_0}{r} - \frac{1}{2}\left(\frac{R_0}{rsin\theta}\right)^2 - \frac{1}{2d}\right]\right]^n \quad (3)$$

The cells in each r-θ slice of a torus is divided into a more refined 10×10 subgrid to better enforce the equilibrium condition in the initial condition. We ensured the stability of the torus by evolving it for over 30 orbits without perturbation and showed that there is no unstable modes.

The torus pressure is computed directly from the torus density, as given by the polytrope equation $P = A\rho^\gamma$. The constant A can be computed by setting $\rho_{max} = 1$, and therefore

$$A = \frac{(d-1)}{2d(n+1)}.$$

The gas density outside the torus (d_0) is chosen to be 10^{-4} and an ambient pressure profile of P=d_0/r is setup in the initial condition. At the boundary of the torus, we compute the torus density compare it with d_0 and take the larger of the two to be the density. This smoothed out the discontinuities due to the piecewise definition of the physical quantities at the boundary of the torus, as shown in the radial profile in Fig. 1 .

A pressure and density floor of either 10^{-8} and 10^{-6} is added in the simulations to prevent numerical artifacts of overflowed floating point that may affect our simulations. Extremely low density gas can appear outside of the torus, when much of the gas has flowed out of the computational domain. The pressure and density floor is several orders of magnitude less than the torus pressure and density, so it is physically negligible in our consideration of the instability.

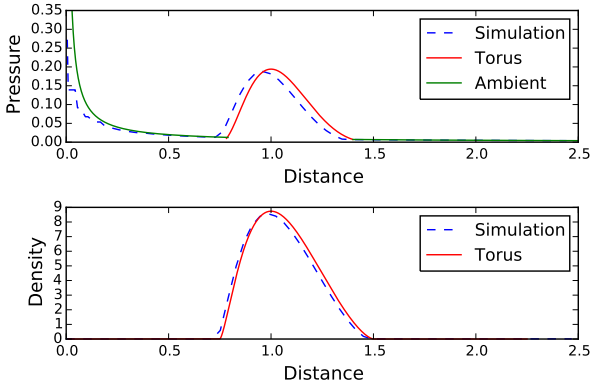

Figure 1. Density and Pressure profile in the initial condition taken from a $\theta = \pi/2$ slice.

2.1.2. *Boundary Condition*

Global instabilities such as the PPI investigated here are often strongly dependent on the choice of boundary condition. Here we adopt the natural choice of periodic boundary condition in the ϕ direction and outflow boundary condition in the outer radial boundary. The inner boundary condition was harder to chose since it can strongly affect the torus during stages of its nonlinear evolution, when the torus spirals in towards the inner boundary. Our choice of the R_0/R_B parameter on the inner boundary of the mesh isolates the central singularity and avoids regions of high gravitational potential as the high infall velocities limit the time steps determined by the Courant Friedrichs Lewy (CFL) condition.

We tested out four combinations of the inner boundary condition by either setting outflowing V_R or V_R=0 and either a corotating boundary or V_θ=V_ϕ=0. The boundary conditions in Run B, D, E restricted the gas from spiraling inwards at later timesteps and results in high velocities that caused the simulation to terminate. Since excess free energy from shearing can drive other types of fluid instabilities, in order to distinctly observe PPI we need to enforce the corotating boundary condition, so that the ghost zone moves with the boundary cells in the active computational domain. Along with setting the outflow radial velocity as zero as the gas hits the inner boundary, the resulting simulation alleviated the high velocities previously observed at the boundaries.

2.2. *Numerical Results*

2.2.1. *Effects of Distortion Parameter*

In Run F, G, we tried using two different distortion parameters that determines the shape of the torus. The value of d=1.1773 is derived from the r_{in} and r_{out} in the A2 slender torus model in Hawley (1991). For qualitative comparison, undistorted torus is smaller with a nearly-circular cross section as d→1. We find that the behavior of the two runs showed similar evolution, however, all

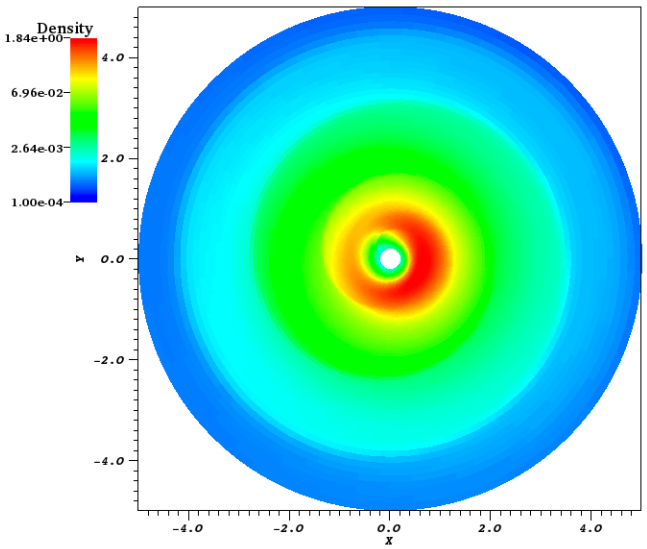

Figure 2. Z-slice of a 3D simulation of the torus showing spiral waves at the nonlinear regime (t=32 orbits).

the sequence of events in Run F occurred earlier in Run G than in Run F.

2.2.2. *Effects of Logarithmic Gridding*

Increasing the radial dynamic range using logarithmic gridding puts more gas into the computational domain so that the ambient conditions remains realistic for a longer period of time after the instability begins the drive the gas outside of the computational domain. Along with the proper boundary conditions as discussed in Sec 2.1.2, we no longer observe low density gas below the 10^{-6} density floor. We attempted at different multiplicative factors of logarithmic gridding in Run H, I, J and found that a factor of 1.03 is sufficient for covering the large radial domain. In Run I and J, the large logarithmic factor results in very fine grids near the inner boundary. Since there is high infall velocities due to the pseudo-Newtonian potential, the CFL condition strongly limits the timesteps of the simulation. In the future, Static Mesh Refinement (SMR) could be used to increase the resolution near the torus mid-plane region.

2.2.3. *Effects of Mode Initialization*

We describe two ways of initializing perturbation in the simulation to trigger the PPI: random initialization and eigenmode initialization. As done in Hawley (1991), for the random initialization, we added a unique, random number scaled by the amplitude to the gas pressure, which effectively adds enthalpy perturbation to each grid zone. For the eigenmode initialization, we added a perturbation of the form $A_0 sin(m\phi)$ in the ϕ-component of the momentum, where A_0 is the amplitude. The comparison between the two initializations can be seen in the mode growth plot in Fig. 7 and 8.

We begin by initializing with amplitude of 1% on the m=1 mode. However, the strong perturbation results in violent, nonlinear evolution within an orbital time. This makes the mode growth analysis difficult as the analytical mode growth derived by Goldreich et al. (1986) is based on a linear stability analysis, which does not give accurate prediction in the nonlinear regime after $t_{saturation}$. The 1% perturbation was acceptable when using the random initialization method because the amplitude of the perturbation does not directly translate into 1% amplitude for the m=1 mode growth. In the random initialization, any frequency mode can be possible, so the percentage of the actual amplitude that contributes to one specific mode amplitude is likely to be lower. Therefore, we decreased the amplitude to 0.001% for the m=1 eigenmode in Run M to conduct the analysis. In both types of initialization, we see strong m=1 mode growth and subsequent higher-order mode growth due to mode coupling.

2.2.4. *Effects of Resolution*

We introduced static mesh refinement in Run N which yielded additional refinement factor of two around the torus. When compared with the uniformly-gridded Run O, we find that the density contours qualitatively converges. The mode growth in m=1 and 2 modes and saturation time also converges. However, the saturation level and the mass accretion rate differs by about a factor of 2∼3 as shown in Fig. 3 and 4.

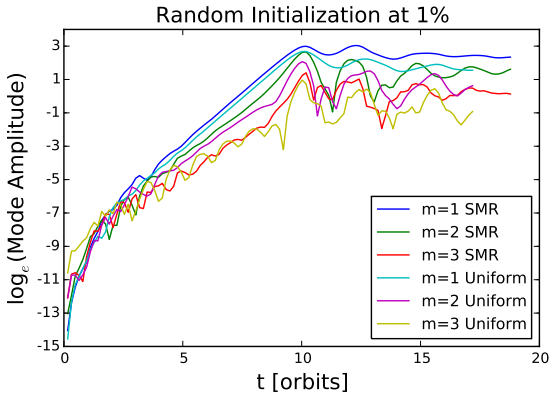

Figure 3. The saturation time and the mode growth rate of the first three modes in Run N and O converges, but their respective saturation levels differ by a factor of 3.

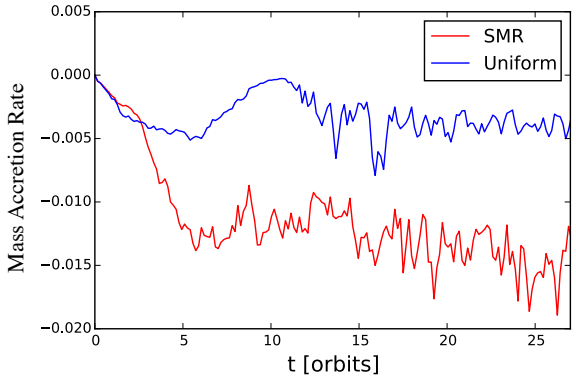

Figure 4. Mass accretion rate history of Run N and O differs by a factor of 3.

One possible reason for this discrepancy is that since we are adding random perturbation on a per-cell basis and different grid resolution (i.e. cell sizes) near the torus region results in different perturbation during initialization. In addition, the higher mass accretion rate in the

Run	Grid	Δr	R_{in}, R_{out}	d	Perturbation	Inner B.C. (r, θ/ϕ)	t_{run} [orbits]	p/d floor
A	$256 \times 96 \times 256$	1.03	0.2,5.0	1.173	Random,1%	0,corotating	33.423	10^{-6}
B	$64 \times 64 \times 64$	1	0.2,2.5	1.173	Random, 1%	0,0	14.961	10^{-8}
C	$64 \times 64 \times 64$	1	0.2,2.5	1.173	Random, 1%	0,corotating	31.672	10^{-8}
D	$64 \times 64 \times 64$	1	0.2,2.5	1.173	Random, 1%	outflow,0	8.117	10^{-8}
E	$64 \times 64 \times 64$	1	0.2,2.5	1.173	Random, 1%	outflow,corotating	7.003	10^{-8}
F	$64 \times 64 \times 64$	1	0.2,2.5	1.125	Random, 0.1%	0,corotating	156.767	10^{-8}
G	$64 \times 64 \times 64$	1	0.2,2.5	1.173	Random, 0.1%	0,corotating	112.841	10^{-8}
H	$96 \times 64 \times 128$	1.03	0.2,5.0	1.173	Random, 1%	0,corotating	56.818	10^{-6}
I	$96 \times 64 \times 128$	1.05	0.2,5.0	1.173	Random, 1%	0,corotating	38.515	10^{-6}
J	$96 \times 64 \times 128$	1.09	0.2,5.0	1.173	Random, 1%	0,corotating	1.592	10^{-6}
K	$256 \times 96 \times 128$	1	0.2,2.5	1.173	Random,0.1%	0,corotating	24.048	10^{-8}
L	$96 \times 64 \times 128$	1.03	0.2,5.0	1.173	m=1, 0.1%	0,corotating	1.76	10^{-6}
M	$96 \times 64 \times 128$	1.03	0.2,5.0	1.173	m=1,0.001%	0,corotating	3.18	10^{-6}
N	$192 \times 128 \times 128$(+one level SMR)	1	0.2,2.5	1.173	Random, 1%	0,corotating	27.375	10^{-6}
O	$192 \times 128 \times 128$	1	0.2,2.5	1.173	Random, 1%	0,corotating	36.128	10^{-6}

Table 1
Selected parameters used in PPI simulations.

Run	Grid	Δr	R_{in}, R_{out}	t_{run} [orbits]
A'	$192 \times 256 \times 1$	1.03	0.2,5.0	8.594
B'	$192 \times 128 \times 128$	1	0.2,2.5	27.375
C'	$192 \times 128 \times 128$	1	0.2,2.5	7.099
D'	$384 \times 256 \times 256$	1	0.2,2.5	10.027

Table 2
Summary of the computational runs for MRI simulations. The run times are generally shorter than in PPI simulations since MHD calculations are computationally expensive. In addition, it is not necessary to evolve the the torus for that long because the instability saturates at around 3 orbits and the behavior qualitatively looks the same in the non linear regime.

higher resolution run may suggest that the lack of resolution suppresses higher-order mode amplitudes, as seen in the lower resolution Run A in Fig.3. Despite using a significantly higher resolution run compared to what had been done previously in Hawley (1990) and Hawley (1991), the lower mode amplitudes in the low resolution may not be sufficient to resolve the higher order modes. However, a more comprehensive resolution study is required to validate this hypothesis.

3. MAGNETOROTATIONAL INSTABILITY

The magnetorotational instability (MRI) is a local, MHD instability that occurs in a differentially-rotating accretion disks where disk is threaded by a weak subthermal, poloidal magnetic field and the angular velocity is decreasing radially outwards. The MRI is now the widely accepted mechanism for outward angular momentum transport in many types of accretion disk systems.

3.1. *Numerical Methods*

Since the MRI is a local instability, many studies have been dedicated to study MRI in a shearing-box approximation. Here, we perform global simulations enable MRI to sample larger wavelength in r and ϕ directions. The computational runs are summarized in Table 2. We used the optimal parameters as discussed in Sec. 2.2 from the PPI run in the MRI simulations: randomly initialized perturbation at 1%, distortion parameter of 1.173, pressure and density floor of 10^{-6}, a corotating boundary in θ, ϕ and outflow boundary condition in the inner radial boundary.

3.1.1. *Initial Conditions*

To initialize an azimuthal field, we make use of the three degrees of freedom to set a convenient gauge of $A_r = A_\phi = 0$ and $A_\phi = \frac{\rho^2}{\beta_0}$. We define initial conditions using the magnetic scalar potential at cell-corners and then compute $B(r, \theta)$ by $\nabla \times A$, rather than directly defining the initial condition using the face-centered magnetic fields to ensure the $\nabla \cdot \vec{B} = 0$ condition is satisfied in the discretized form. Using Stoke theorem to convert the $\vec{B}$ equation into an integral form,

$$\int \vec{B} \cdot d\vec{S} = \int A \cdot dl \tag{4}$$

we can get the magnetic field by the simple discrete form:

$$\vec{B} = \frac{1}{\Delta S}[A_{\phi,+} l_+ + A_{\phi,-} l_-]. \tag{5}$$

β_0 is a user-defined value for the plasma beta describing the ratio of gas-to-magnetic pressure. To maintain the initial hydrostatic equilibrium of the torus, we need to chose a β such that the initial azimuthal magnetic field is weak. Additionally, β is important in determining the number of zones required to resolve MRI per scale height of the system. The instability requires a rotational velocity profile where the inner portion of the disk is rotating faster than the outer part of the disk, as explained in Sec.4.1.

3.2. *Numerical Results*

3.2.1. *Effects of Resolution*

Since the MRI is dominated by higher-order modes, as shown in Sec.9, it is crucial that our grids resolve to scales smaller than these in order for to resolve these short wavelength modes. The scale height (H) in our simulation decreases radially outward as $\sqrt{2/r}$. We use the zones-per-scale-height formula in Hawley et al. (2011) to compute the minimum zones (N) required in the r direction to resolve the MRI and obtained N_ϕ=223.713. Therefore, we ran a high-resolution simulation with $384 \times 256 \times 256$ on 768 processors. However, we did not find qualitative differences between the the higher resolution Run D' and lower resolution Run C' because all the modes were growing at approximately the same rate. Quantitatively, our linear-fit and Eq. 13 methods were unable to give an accurate estimate of the

mode growth rate because the instability saturates too quickly at around three orbits. Therefore we could not test the effect of resolution on the development of MRI.

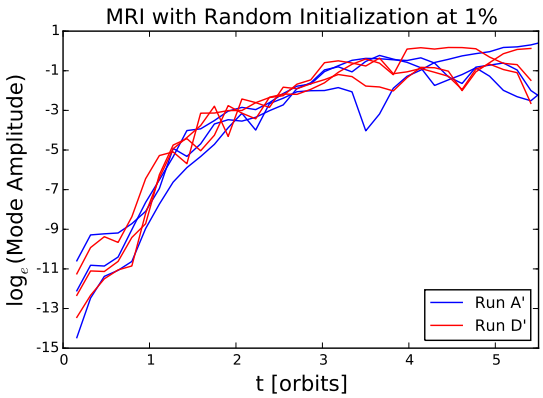

Figure 5. Mode growth rate and saturation level of the first three modes in Run A' and D' qualitatively converges.

4. COMPARISON OF INSTABILITIES

4.1. *Physical Mechanism*

PAPALOIZOU-PRINGLE INSTABILITY

Based on the torus boundaries on the z=0 plane in (Papaloizou and Pringle 1984),

$$\tilde{\omega}_{\pm} = \frac{\tilde{\omega_0}}{1 \mp \sqrt{1 - \frac{1}{d}}} \tag{6}$$

where d is the distortion parameter, we obtained $(\tilde{\omega}_+, \tilde{\omega}_-) = (1.623, 0.723)$ for the case of a slender torus. Therefore, the scaled azimuthal wavenumber β is related to the wave mode by $\beta = 0.45m$. For the m=1 modes, since the condition $\beta < 0.59$ is satisfied, it falls into the class of unstable modes known as the principle branch which has its corotation radius R_c at pressure maximum. Goldreich et al. (1986) showed that these can be reasonable approximated with a set of 2D height-integrated equations. The corotation radius (R_c) is the radius where the angular speed (Ω)is equal to the pattern speed(Ω_p), where the pattern speed is described $Re(\omega)/m$. R_c separates the inner region of the torus with negative action the outer region with positive action.

For the principal modes, the instability comes from the coupling between two traveling surface waves launched from the inner and outer edge of the torus. More generally, for higher-order modes, Narayan et al. (1987) describes amplification mechanism where the transmitted and reflected wave gets trapped near the evanescent region around R_c. With a satisfied phase condition, this amplification mechanism creates a feedback loop that reflects its own output back into the system, thus triggering the unstable mode growth seen in PPI. The principal mode is a special case of higher-order modes where the whole torus is the evanescent region, so the only waves that could interact and grow unstable are the traveling surface waves near the perfectly reflecting boundaries of $\tilde{\omega_{\pm}}$.

MAGNETOROTATIONAL INSTABILITY

The MRI can also be explained from the linear stability analysis of the MHD equations, as detailed in the review paper by Balbus and Hawley (1998). The analysis yields a stability criterion for the rotational velocity profile:

$$(\vec{k} \cdot \vec{u_A})^2 > -\frac{d\Omega^2}{dlnR} \tag{7}$$

$$\frac{d\Omega^2}{dlnR} > 0 \tag{8}$$

Simplifying this by chain rule,

$$\Omega \frac{d\Omega}{dlnR} > 0 \tag{9}$$

In disks which rotates in one direction throughout,

$$\frac{d\Omega}{dR} > 0 \tag{10}$$

This suggest that the instability arises whenever the angular velocity is decreasing radially outward, which is true for observed Keplerian disks.

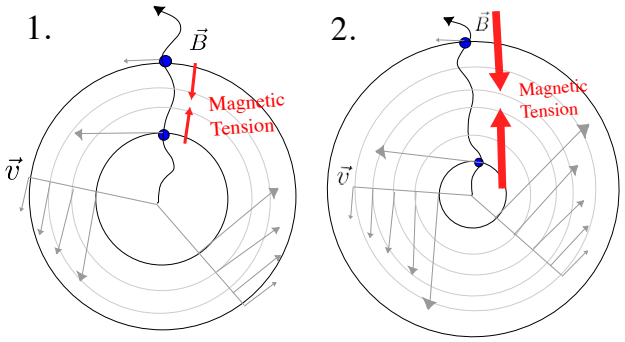

Figure 6. A simplified picture showing how the MRI works.

This criterium makes sense in terms of the mechanical picture as shown in Fig. 6. The magnetic tension force exerted by the poloidal magnetic field line connecting the two fluid elements exert an effective angular momentum transfer outwards. Therefore, the inner fluid element drops to a lower orbit and the outer fluid element is boosted up to a higher orbit. The larger separation distance between the fluid elements result in a stronger magnetic tension and the process eventually snowballs into a runaway instability.

4.2. *Mode Growth Analysis*

In order to quantify the results of the numerical simulation, we conduct the mode growth analysis and compare our result with the 3D numerical simulations done in Hawley (1990) and Hawley (1991) and the analytical growth rates given by Goldreich et al. (1986). To motivate the analysis of the eigenmodes, we first consider the physical mechanisms that give rise to PPI summarized in Narayan and Goodman (1989).

The PPI give rise to unstable was modes that grows exponentially in time. We quantify the mode amplitudes by conducting a Fourier decomposition in the ϕ direction. The number of zones in the ϕ direction was chosen for this purpose to powers of two in order to speed up the Fast Fourier Transform (FFT) algorithm used to extract the modes.

We use a Python package `h5py` to read in the simulation data stored in HDF5 format per timestep. For every meshblock the datafile, we first compute the mass enclosed per cell in each $\Delta\phi$ slice by :

$$\frac{\mathrm{M_{enclosed}}}{\Delta\phi} = \rho\Delta V_{\mathrm{cell}} = \rho r^2 sin\theta\Delta r\Delta\theta \tag{11}$$

$$D(\phi) = \sum_r \sum_\theta \rho\frac{\Delta V_{\mathrm{cell}}}{\Delta\phi} \tag{12}$$

Due to the z-ordering in *Athena++'s* internal data structure, we use the the logical locations stored in each meshblock and sum over all the mass in a particular $r-\theta$ slice. This yields a 1D-array of length 128 containing the integrated mass per slice, $D(\phi)$. Then by Fourier decomposing the wave into 128 bins, we compute the magnitude by $|A| = \sqrt{\tilde{A}\cdot\tilde{A}^*}$.

We compute the mode growth rate by a linear least square fit on the log-amplitude plot and separately by Eq.13. Since we assume the form of the physical quantity to be $q(t) = q_0 e^{\frac{t}{\tau}}$ in the linear stability analysis, we can compute the mode growth by :

$$\tau = \frac{\Delta t}{log(\frac{x(t)}{x_0})} \tag{13}$$

We use the crude method of chi-by-eye to select the range of the linear region and find that these two methods yield simmilar results; however, Eq. 13 can be an inaccurate estimate if the start and end point lie near a local extremum.

PAPALOIZOU-PRINGLE INSTABILITY

From Fig. 7 and 8, we see a very strong m=1 mode growth in the linear regime. At around 6 orbits, the m=1 mode begins to couple with the higher order modes, resulting in a sharp subsequent mode growth. The instability saturates around 10 orbits. This saturation level is consistent over all the resolution that we tested, which suggests a physical origin of the saturation. One possible reason that explains the saturation suggested by Gat and Livio (1992) is the loss of an inner reflecting boundary at the onset of accretion and development of the spiral pressure wave, which disrupts the corotation amplification mechanism. Table 3 summarizes the mode growth comparison with Hawley (1990) for the random and eigenmode (m=1) initialization.

	Random Initialization		Eigenmode Initialization	
m=1	0.8679	0.855	0.2667	0.2621
m=2	0.4701	0.211	0.5505	0.5100
m=3	0.3756	0.254	0.6828	0.6820

Table 3
Left-flushed values are the mode growth in Run J, M respectively; right-flushed values are mode growth in Hawley (1991).

MAGNETOROTATIONAL INSTABILITY

We were unable to compare the mode growth rates with other previous studies because 1) most of the MRI works that we reviewed were shearing box simulations which did not contain global ϕ mode information and 2) since the MRI saturated really quickly it was hard to find an reliable linear regime to compute the mode growth rate. Even though the ϕ-direction mode growth analysis fails to characterize some of the higher mode growth for MRI in the r-θ direction, we nevertheless use Fig. 8 to compare with with the dominant m=1 mode in thePPI case of Fig. 3 and demonstrate the importance of the higher order modes in contributing to MRI.

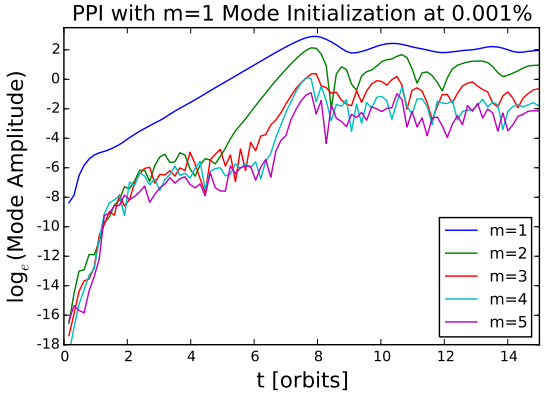

Figure 7. Run M's mode growth of the m=1-5 modes.

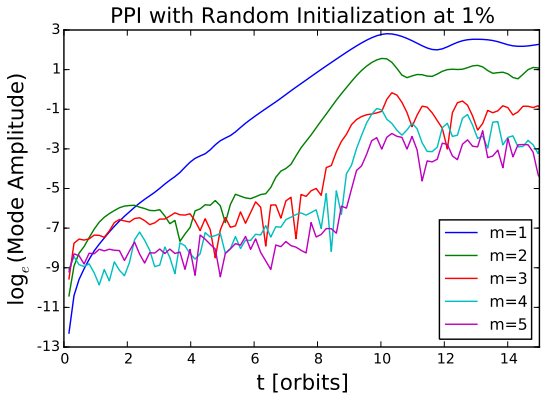

Figure 8. Run J's mode growth of the m=1-5 modes.

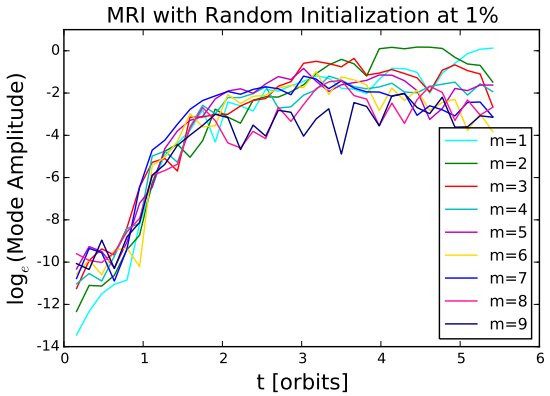

Figure 9. Mode growth of the m=1-9 initialized for the MRI case.

4.3. *Mass Accretion History*

We compute the accretion onto the inner boundary by computing the mass flux that incidents the innermost cells.

$$\frac{dM}{dt} = \sum_{j,k} \rho v_r \Delta S_{i,j\pm,k} \tag{14}$$

As shown in Fig.10, the mass accretion rate history in our MRI simulation qualitatively agrees with the accretion rate history in Jiang et al. (2014). In addition, we find that the mass accretion rate in the MRI case is much stronger than that of the PPI.

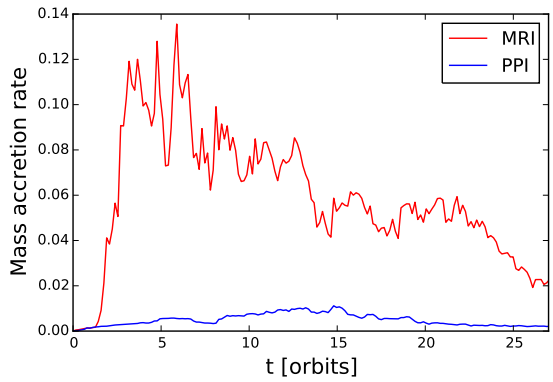

Figure 10. The mass accretion rate onto the inner boundary that results from the instabilities.

5. CONCLUSION

In this study, we use the *Athena++* code to investigate the effects of magnetorotational instability (MRI) and Papaloizou-Pringle Instability (PPI) on accretion disk tori. We investigate a variety of physical parameters such as the effects of torus distortion, different methods for mode initialization and found that the simulation results agrees with the physical picture of how the instability works. Other physically interesting parameter to consider but not investigated in these study is the effect of the plasma beta and compressibility on the stability of the torus, as has been done in previous analytical and numerical studies.

We make use of various code features in *Athena++* such as logarithmic gridding and static mesh refinement to improve the simulation and minimize numerical effects. We investigate the numerical effect of changing the resolution, boundary conditions, the density/pressure floor, and the size of the computational domain and find that the physical outcomes of the instabilities qualitatively converges. However, for the PPI case, our quantitative mode growth analysis showed that only the mode growth rate and the saturation time converges, but not the mass accretion history and the saturation level, which suggests that a greater resolution may be necessary for capturing higher order modes. Nevertheless, the general success of these simulations in reproducing the analytical and numerical results found in previous literature demonstrate the robustness of the *Athena++* code in handling these two test cases.

From the mass accretion history of the two instabilities, it is evident that the MRI is significantly more effective in angular momentum transport than PPI. In addition, the setup of MRI is more astrophysically-realizable than that of the constant-angular momentum condition enforced by PPI. The MRI simply requires a weak toroidal magnetic field and outwardly decreasing angular velocity condition which is physically-plausible in the micro-Gauss-level magnetic fields in the interstellar medium and observed rotational profiles of Keplerian disks. The combination of these factors explains the recent interest in studying the MRI as a mechanism for generating the turbulent viscosity necessary for outward angular momentum transport in accretion disk systems.

ACKNOWLEDGMENTS

I am sincerely thankful for mentoring and support from Kengo Tomida and Jim Stone throughout this summer project. This research used resources of the National Energy Research Scientific Computing Center, a DOE Office of Science User Facility supported by the Office of Science of the U.S. Department of Energy under Contract No. DE-AC02-05CH11231.

REFERENCES

J. C. B. Papaloizou and J. E. Pringle, MNRAS **208**, 721 (1984).
J. C. B. Papaloizou and J. E. Pringle, MNRAS **213**, 799 (1985).
J. F. Hawley, ApJ **356**, 580 (1990).
P. Goldreich, J. Goodman, and R. Narayan, MNRAS **221**, 339 (1986).
J. F. Hawley, ApJ **381**, 496 (1991).
O. M. Blaes, MNRAS **227**, 975 (1987).
J. F. Hawley, X. Guan, and J. H. Krolik, ApJ **738**, 84 (2011).
R. Narayan, P. Goldreich, and J. Goodman, MNRAS **228**, 1 (1987).
S. A. Balbus and J. F. Hawley, Reviews of Modern Physics **70**, 1 (1998).
R. Narayan and J. Goodman, in *NATO Advanced Science Institutes (ASI) Series C*, edited by F. Meyer (1989), vol. 290 of *NATO Advanced Science Institutes (ASI) Series C*, p. 231.
O. Gat and M. Livio, ApJ **396**, 542 (1992).
Y.-F. Jiang, J. M. Stone, and S. W. Davis, ApJ **796**, 106 (2014).